Spurious Beam Suppression in Dual-Beam Phased Array Transmission by Impedance Tuning

Pedro Rodriguez-Garcia, Jack Sifri, Caleb Calabrese, Adam Goad, Charles Baylis, and Robert J. Marks II

ABSTRACT A significant challenge for dual-beam, co-designed systems, such as for simultaneous radar and communications transmission, has been identified as the spurious beams produced by spatial intermodulation from nonlinearities in the transmitter power amplifier. We demonstrate that tuning the load impedance of the power amplifiers can reverse the element-wise power amplifier nonlinear distortion, reducing the magnitude of the unwanted beam transmissions and restoring the integrity of the dual-beam antenna pattern for application to an active electronically scanned array (AESA). A comparison to a recently documented predistortion approach for correcting spurious transmissions is provided, and it is shown that impedance tuning can address both element output power and linearity, whereas predistortion addresses only the linearity issue and causes the amplifier gain in many of the array elements to suffer. For multiple dual-beam angle scenarios, simulation results show that impedance tuning is effective at maximizing beam power in both beam directions, maximizing current gain in the element power amplifiers, and minimizing the size of the unwanted spurious beams.

I. INTRODUCTION

Dual-beam wireless transmissions are often performed from phased-array systems. One example is the simultaneous transmission of radar and communication signals in different directions [1]. This provides a significant benefit to radar systems in an era where spectrum sharing has been forced upon many radars, and bandwidth allowing good range detection is difficult to obtain. Multi-beam transmissions rely on spatial diversity to avoid interference, and allow frequencies to be shared by more than one user, easing the strain on the frequency spectrum. Nonlinearities in the power amplifiers (PAs) of the transmit elements, however, cause unwanted spatial intermodulation beams, or "beat beams", to be transmitted [2, 3]. Hemmi describes combined spatial and frequency intermodulation products from a dual-beam, dual-tone transmission [4], later discussed by Haupt [5]. Mollen uses Volterra and Hermite PA modeling approaches to calculate intermodulation beams [6]. Experimental measurement demonstration of intermodulation array products is provided by Zaghloul for a Ku-band array [7]. Loyka discusses modeling and simulation techniques related to active array performance and suggests the instantaneous quadrature technique to capture circuit nonlinearities and their effects on array performance [8]. Obermier discusses an approach to assess the effects of spatial intermodulation on the antenna array factor, and to adjust the input power needed to maximize the equivalent isotropic radiated power (EIRP) [9]. While we consider the specific problem of transmitter beam intermodulation, Kaho describes an intermodulation beam phenomenon that can occur based on single-beam transmission of two different carrier frequencies, and demonstrates a method of improving the intermodulation beams by adjusting the carrier to intermodulation power ratio of the PA [10]. Further, intermodulation issues in receive arrays and potential solutions are discussed and demonstrated by Rupakula [11].

To our knowledge, we present the first consideration of impedance tuning as a strategy for spatial intermodulation beat beam mitigation in dual-beam transmission. Recent demonstrations of high-power reconfigurable impedance matching circuits for radar [12, 13] and application of impedance tuning to single-beam array transmissions [14] suggest that future implementation of impedance tuning may be feasible for minimization of spatial intermodulation products in a dual-beam shared-frequency transmission system. Since impedance tuning impacts both the gain and linearity of the PA, the approach we present can deal with the undesirable beat-beam artifacts of the amplifier nonlinearities while also maximizing element amplifier gain, a combined task that most waveform engineering and predistortion techniques alone cannot accomplish. Various works in the literature deal with linearity issues, mitigating the undesirable beat beams through waveform engineering, orthogonal phase distribution selection, and an amplifier-modeling based approach [15]-[19]. Peccarelli provides a survey of techniques to mitigate spatial interference and effects of transceiver nonlinearities [20]. Dunn describes the use of a predistortion approach to mitigate spectral spreading based on nonlinearities that change with changing antenna impedance resulted from array scanning [21]. Braithwaite describes a predistortion approach to mitigate the unwanted intermodulation beams [22]. While impedance tuning has been demonstrated as a solution for control of spectral intermodulation products for coexistence [23], we are presenting the first demonstration

of using impedance tuning to control spatial intermodulation products. We utilize a co-simulation technique with circuit and electromagnetic (EM) simulators to compute the effect on array performance from nonlinearities in the amplifier. We compare the results of our technique to a recently demonstrated predistortion method [22], and show that impedance tuning is much more effective at obtaining the desired beam pattern while maximizing element PA gain.

.

II. SPATIAL INTERMODULATION THEORY

Consider a dual-beam, shared-frequency transmission block diagram, as shown in Fig. 1. Both beams share the same frequency ω_0. In this case, the beams are labeled as "radar" and "communications" beams, but because modulations are not considered, this is really a generic dual-beam transmission example. The input signals for the two beams are added together at each element's power amplifier [4] after applying the appropriate phase shifts.

In the following development, the two beams transmitted are labeled as "radar" and "communication", but this actually is a simple, generic dual-beam system and can apply to general dual-beam problems, as modulation is not considered at this level of the work. The general time-domain current expression can be written as follows:

$$i_{i,n}(t) = b_{r_n}(t)\cos(\omega_0 t - nk_0 d\sin\theta_r + \phi_r(t)) + b_{c_n}(t)\cos(\omega_0 t - nk_0 d\sin\theta_c + \phi_c(t)) \quad (1)$$

where $b_{r,n}(t)$ and $\phi_r(t)$ are the amplitude and phase modulations of the radar signal, respectively, and $b_{c,n}(t)$ and $\phi_c(t)$ are the amplitude and phase modulations of the communication signal, respectively. The $-nk_0 d\sin\theta_r$ term allows the intended modulated radar signal to be properly received at the θ_r elevation angle, and the $-nk_0 d\sin\theta_r$ term allows the intended modulated communication signal to be properly received at the θ_c elevation angle. d is the antenna element spacing, and $k_0 = 2\pi/\lambda_0$, where λ_0 is the wavelength.

Examination of (1) shows that the amplitude and phase modulation of the communication and radar signals cause the total current $i_{i,n}(t)$ to change in time on the order of the modulating signal changes. For simple analog modulation based on audio signals, the message can contain frequency content up to approximately 20 kHz. This means that the rate of change of the current is on the order of 1/20,000 = 50 µs. For digital modulations associated with fourth-generation Long-Term Evolution (4G LTE) waveforms, Ghayas states that the bits-per-second rate for 64-symbol quadrature amplitude modulation (64-QAM) is typically near 75 MBits/s for the uplink and near 300 Mbits/second for the downlink. Because 6 bits are used in 64-QAM, this gives a symbol rate of approximately 12.5 Megasymbols/second for the uplink and 50 Megasymbols/second for the downlink. In the fast case (downlink), the symbol changes every 1/50,000,000 seconds = 20 ns. In the slower, uplink case, the symbol changes every 1/12,500,000 = 80 ns. These fast variations in the modulation cause the amplifier drive levels to change in the different array elements, since these currents are the superpositions of the radar and communications components. While this may initially strike the reader as prohibitive, Egbert has been shown that impedance tuners can be effectively used in scenarios that change orders of magnitude faster than the tuner tuning capabilities, showing that optimization for average power in a quickly changing spectrum-sharing radar can be performed by optimizing for average power rather than instantaneous power [24]. The demonstration of fast impedance tuning in real-time, multi-beam transmission will be left for future work.

The point of this paper is to show that impedance tuning, if it can be performed properly and quickly, can remove unwanted spurious beams in dual-beam transmission, providing a foundation for the development of advanced impedance tuning techniques to optimize in dual-beam transmission scenario with consideration of the message signals. This paper presents fundamental research to be used as a "stepping-stone" to an implementable approach; it merely shows that impedance tuning makes a difference, but does not consider the implementation of an actual tuning algorithm into a real system.

For purposes of this paper, the simple case of unmodulated signals will be considered, appropriate if the modulations are slow-time processes in comparison to the impedance tuning operation (discussed above). As such, this is not a completed radar-communication system because the modulations are not considered (as aforementioned). In this case, the amplitude and phase modulation values are constant in equation (1):

$$i_{i,n}(t) = B_{r,n}\cos(\omega_0 t - nk_0 d\sin\theta_r + \phi_r) + B_{c,n}\cos(\omega_0 t - nk_0 d\sin\theta_c + \phi_c) \quad (1b)$$

Because the amplitude and phase terms are constant in time, this expression can be rewritten in phasor notation, where the time-dependent signal is defined in terms of the phasor as

$$i_{i,n}(t) = \mathrm{Re}\left(I_{i,n}e^{j\omega_0 t}\right) \quad (2)$$

Using (1a) and (2) gives the phasor as

$$I_{i,n} = B_{r_n}e^{j\phi_r}e^{-jnk_0 d\sin\theta_r} + B_{c_n}e^{j\phi_c}e^{-jnk_0 d\sin\theta_c} \quad (3)$$

or

$$I_{i,n} = A_{r_n}\mathrm{e}^{-jn\alpha_r} + A_{c_n}\mathrm{e}^{-jn\alpha_c} = I_{r_n} + I_{c_n}, \quad (4)$$

where $A_{r_n} = B_{r_n}e^{j\phi_r}$, $A_{c_n} = B_{c_n}e^{j\phi_c}$, $\alpha_r = k_0 d\sin\theta_r$, and $\alpha_c = k_0 d\sin\theta_c$. From (2) it follows that

$$i_{i,n}(t) = \frac{1}{2}\left(I_{i,n}e^{j\omega_0 t} + I_{i,n}^{*}e^{-j\omega_0 t}\right) \quad (5)$$

The third-order nonlinearity artifacts can be explored

by placing this time-domain input to a system with the input-output current characteristic given by

$$i_{o,n}(t) = \beta_1 i_{i,n}(t) + \beta_2 i_{i,n}^2(t) + \beta_3 i_{i,n}^3(t). \quad (6)$$

The square and cube of the time-domain input current are

$$i_{i,n}^2(t) = \frac{1}{4}\left[I_{i,n}^2 e^{j2\omega_0 t} + 2\left|I_{i,n}\right|^2 + \left(I_{i,n}^*\right)^2 e^{-j2\omega_0 t}\right] \quad (7)$$

$$\begin{aligned} i_{i,n}^3(t) = \frac{1}{8}\Big[&I_{i,n}^3 e^{j3\omega_0 t} + 3\left|I_{i,n}\right|^2 I_{i,n} e^{j\omega_0 t} \\ &+ 3\left|I_{i,n}\right|^2 I_{i,n}^* e^{-j\omega_0 t} \\ &+ \left(I_{i,n}^*\right)^3 e^{-j3\omega_0 t}\Big] \end{aligned} \quad (8)$$

Thus equation (6) gives the time-domain output as

$$\begin{aligned} i_{o,n}(t) = &\frac{1}{2}\beta_1\left(I_{i,n}e^{j\omega_0 t} + I_{i,n}^* e^{-j\omega_0 t}\right) \\ &+ \frac{1}{4}\beta_2\left[I_{i,n}^2 e^{j2\omega_0 t} + 2\left|I_{i,n}\right|^2 \right. \\ &\left. + \left(I_{i,n}^2\right)^2 e^{-j2\omega_0 t}\right] \\ &+ \frac{1}{8}\beta_3\left[I_{i,n}^3 e^{j3\omega_0 t} + 3\left|I_{i,n}\right|^2 I_{i,n} e^{j\omega_0 t}\right. \\ &+ 3\left|I_{i,n}\right|^2 I_{i,n}^* e^{-j\omega_0 t} \\ &\left. + \left(I_{i,n}^*\right)^3 e^{-j3\omega_0 t}\right] \end{aligned} \quad (9)$$

Since the problem being examined is the problem of spatial spurious beams at the frequency ω_0, the terms associated with the frequency ω_0 will be considered, and labeled with the expression $i_{o,n}^{imd3}(t)$:

$$\begin{aligned} i_{o,n}^{imd3}(t) = &\frac{1}{2}\beta_1\left[I_{i,n}e^{j\omega_0 t} + I_{i,n}^* e^{-j\omega_0 t}\right] \\ &+ \frac{3}{8}\beta_3\left[\left|I_{i,n}\right|^2 I_{i,n} e^{j\omega_0 t}\right. \\ &\left. + \left|I_{i,n}\right|^2 I_{i,n}^* e^{-j\omega_0 t}\right] \end{aligned} \quad (10)$$

This expression can be rewritten as

$$i_{o,n}^{imd3}(t) = \mathrm{Re}\left\{\left(\beta_1 I_{i,n} + \frac{3}{4}\beta_3\left|I_{i,n}\right|^2 I_{i,n}\right)e^{j\omega_0 t}\right\} \quad (11)$$

This defines the related phasor as

$$I_{o,n}^{imd3} = \beta_1 I_{i,n} + \frac{3}{4}\beta_3\left|I_{i,n}\right|^2 I_{i,n} \quad (12)$$

Using (4) for $I_{i,n}$ gives

$$\begin{aligned} \left|I_{i,n}\right|^2 = &\left|A_{r_n}\right|^2 + A_{r_n}A_{c_n}^* e^{-jn\alpha_r} e^{jn\alpha_c} \\ &+ A_{c_n}A_{r_n}^* e^{-jn\alpha_c} e^{jn\alpha_r} + \left|A_{c_n}\right|^2 \end{aligned} \quad (13)$$

and

$$\begin{aligned} \left|I_{i,n}\right|^2 I_{i,n} = &\left|A_{r,n}\right|^2 A_{r,n} e^{-jn\alpha_r} + 2\left|A_{c,n}\right|^2 A_{r,n} e^{-jn\alpha_r} \\ &+ 2\left|A_{r,n}\right|^2 A_{c,n} e^{-jn\alpha_c} \\ &+ \left|A_{c,n}\right|^2 A_{c,n} e^{-jn\alpha_c}. \end{aligned} \quad (14)$$

Using (14) with (12) gives the phasor output current component at the frequency ω_0 as

$$\begin{aligned} I_{o,n}^{imd3} = &A_{r_n}\left(\beta_1 + \frac{3}{4}\beta_3\left|A_{r_n}\right|^2 + \frac{3}{2}\beta_3\left|A_{c_n}\right|^2\right)e^{-jn\alpha_r} \\ &+ A_{c_n}\left(\beta_1 + \frac{3}{4}\beta_3\left|A_{c_n}\right|^2\right. \\ &\left. + \frac{3}{2}\beta_3\left|A_{r_n}\right|^2\right)e^{-jn\alpha_c} \\ &+ \frac{3}{4}\beta_3 A_{r_n}^2 A_{c_n}^* e^{-jn(2\alpha_r - \alpha_c)} \\ &+ \frac{3}{4}\beta_3 A_{c_n}^2 A_{r_n}^* e^{-jn(2\alpha_c - \alpha_r)} \end{aligned} \quad (15)$$

The β_3 term is a parameter that models the gain compression of the PA and is typically modeled as a negative number [25]. This term describes the generation of third-order nonlinearities that appear in the output signal of the PA. With a negative β_3 term, as is the case when a compressed PA is connected to the individual antenna elements, the amplitude of the phasor signal is reduced, indicating that some power is lost at the fundamental frequency ω_0 to third-order IM distortion (IMD3).

While the terms at the fundamental frequency do not contain β_2, it should be noted that the second-order nonlinearity term is not completely inconsequential: it can result in generation of unwanted spurious products in the upconversion of the I/Q symbols if a direct-conversion transmitter is used. This effect has been noted by James and Fulton, along with a solution involving spatial decorrelation using local-oscillator outphasing [26].

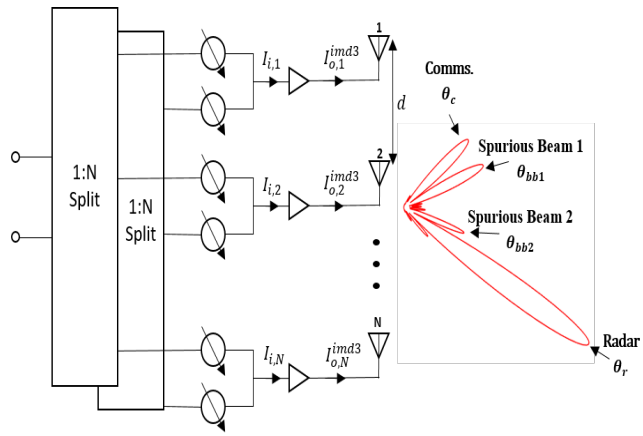

Fig. 1. Dual-beam, dual-signal, shared-frequency phased array RadCom block diagram.

The IMD3 products are included in the PA output signal fed to the individual antenna elements in the array, causing distortion in the far-field array pattern. The far-field array factor determines the output beam pattern of the phased array. In a uniform linear array (ULA) consisting of N antenna elements as shown in Fig. 2, the array factor is derived by the relative positions and spacings of the antenna elements and the direction of wave propagation caused by the individual element excitations. A boresight reference is used for the elevation angle, θ.

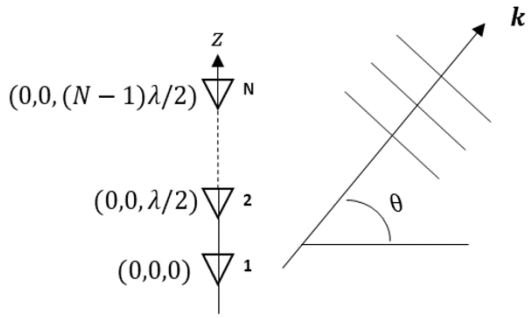

Fig. 2. Array of N elements placed along z-axis separated in distance by $\lambda/2$.

Each nth antenna element is located at a position given by $\boldsymbol{r}_n = (x_n, y_n, z_n)$, and the wave propagation vector is given by $\boldsymbol{k} = k_0(\hat{x}\cos\theta\cos\phi + \hat{y}\cos\theta\sin\phi + \hat{z}\sin\theta)$. Since each element is excited with the PA output signal described by (3), the array factor is the spatial Fourier Transform in the far-field of the phasor excitation signals fed to the radiating antenna elements:

$$AF(\theta) = \sum_{n=1}^{N} I_{o,n}^{imd3} e^{j\boldsymbol{k}\cdot\boldsymbol{r}_n}. \qquad (16)$$

Expanding this array factor in (16), for an array located on the z axis ($x_n = 0$ and $y_n = 0$) yields the IMD3 array factor radiating superposition in the $\phi = 0°$ cut given by

$$\begin{aligned} &AF(\theta)_{imd3} \\ &= \sum_{n=0}^{N-1} A_{r_n}\left(\beta_1 + \frac{3}{4}\beta_3\left|A_{r_n}\right|^2 \right. \\ &\left. + \frac{3}{2}\beta_3\left|A_{c_n}\right|^2\right) e^{j(n[k_0 d\sin(\theta)-\alpha_r])} \\ &+ \sum_{n=0}^{N-1} A_{c_n}\left(\beta_1 + \frac{3}{4}\beta_3\left|A_{c_n}\right|^2 \right. \\ &\left. + \frac{3}{2}\beta_3\left|A_{r_n}\right|^2\right) e^{j(n[k_0 d\sin(\theta)-\alpha_c])} \\ &+ \frac{3}{4}\beta_3 \sum_{n=0}^{N-1} A_{r_n}^2 A_{c_n}^* \, e^{j(n[k_0 d\sin(\theta)-(2\alpha_r-\alpha_c)])} \\ &+ \frac{3}{4}\beta_3 \sum_{n=0}^{N-1} A_{c_n}^2 \, A_{r_n}^* \, e^{j(n[k_0 d\sin(\theta)-(2\alpha_c-\alpha_r)])}, \end{aligned} \qquad (17)$$

The resulting array pattern at frequency ω_0 will have four large-magnitude beams: two intentional main beams at θ_r and θ_c and two spurious spatial intermodulation beams at θ_{bb1} and θ_{bb2}. These spurious beam locations are derived as follows from (17):

$$\alpha_{bb_1} = 2\alpha_c - \alpha_r\,, \alpha_{bb_2} = 2\alpha_r - \alpha_c, \qquad (18)$$

$$\theta_{bb_1} = \sin^{-1}\left(-\frac{\alpha_{bb_1}}{k_0 d}\right), \theta_{bb_2} = \sin^{-1}\left(-\frac{\alpha_{bb_2}}{k_0 d}\right), \qquad (19)$$

The quantities in (18) describe the IMD3 phase distortions caused by the PA nonlinearities at the fundamental frequency ω_0 to the antenna feed signals. Equation (19) calculates the directions in which these unintended spurious beams are transmitted in the far-field. Figs. 3-5 show the theoretical elevation antenna pattern of a 64-element $\lambda/2$-spaced linear array for several RadCom direction combinations with and without the calculated third-order power amplifier nonlinearities, calculated from (16) and plotted using Matlab. For purposes of generating these simple plots, the assigned values are $\beta_1 = 1.5$ and $\beta_3 = -0.5$ for the plots where the PA is present. Without the PA, there is no nonlinearity present, and the constant β_3 term is set to 0. Without the intermodulation terms in (6), the array factor contains only the intended radar and communication beam terms. In Figs. 3-5, the array patterns without the PA show pronounced transmission beams only at θ_r and θ_c.

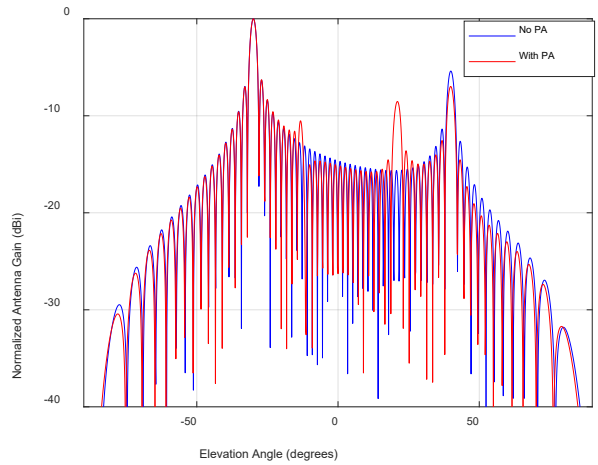

Fig. 3. Normalized theoretical elevation dual-beam array pattern (dBi): $\theta_r = -30°$, $\theta_c = +40°$, calculated $\theta_{bb1} = -12°$, calculated $\theta_{bb2} = +21°$.

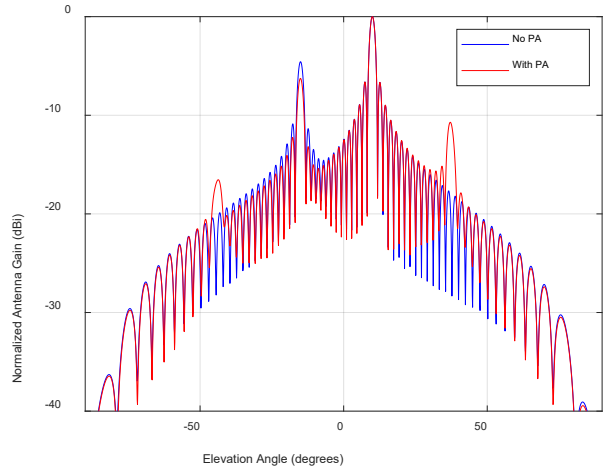

Fig. 4. Normalized theoretical elevation dual-beam array pattern (dBi): $\theta_r = +10°$, $\theta_c = -15°$, calculated $\theta_{bb1} = -44°$, calculated $\theta_{bb2} = +37°$.

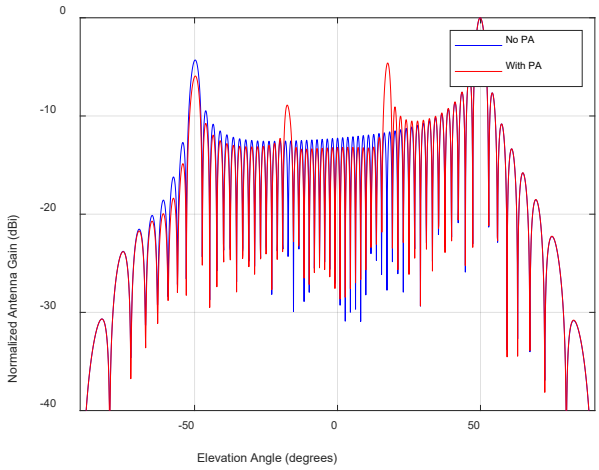

Fig. 5. Normalized theoretical elevation multi-beam antenna pattern: $\theta_r = +50°$, $\theta_c = -50°$, calculated $\theta_{bb1} = -17°$, calculated $\theta_{bb2} = +17°$.

When the IMD3 artifacts are ignored, the antenna array transmits the two intended main beams at their respective elevation locations. When the IMD3 artifacts are included, however, two additional undesired beams are transmitted. In Fig. 3, the elevation angles of the radar and communications beams are θ_r = - 30° and θ_c = + 40°, respectively. From (19), the spurious beams resulting from IMD3 are calculated to be at θ_{bb1} = -12° and θ_{bb2} = +21°. The plot of the array pattern with the PAs present shows new beam presence around these angles. The theory was similarly verified in the scenarios of Figs. 4 and 5, with new beams visible at θ_{bb1} and θ_{bb2}. All plots showed the theoretical results of a 64-element $\lambda/2$-spaced ULA which showed pronounced spurious beams at approximately the expected directions, as calculated by equation (19). When more elements are used, the spurious beams become more pronounced, since more elements provide sharper resolution due to increased far-field spatial sampling described by equation (16). When fewer antenna elements are used, the spurious beams are less pronounced, and may be fused into the adjacent sidelobes in the array pattern due to imprecise far-field spatial sampling.

III. SPATIAL INTERMODULATION SUPPRESSION

To view and correct the issue of spatial modulation in a more realistic setting, a joint circuit and electromagnetic (EM) simulation platform was used. Using the Advanced Design System software (ADS) and ADS Momentum EM simulator from Keysight Technologies, a schematic was generated with an array of 16 $\lambda/2$-spaced microstrip patch antenna elements. The elements were designed using Rogers RO4003C substrate at the design frequency of 3.55 GHz, to lie within the 3.55-3.7 GHz radar band, presently allocated for spectrum sharing between radar and communications. As in the system block diagram of Fig. 1, the antenna array is fed using two signal sources: one for each beam's signal. These sources are connected to two 1:16 power splitters that feed into phase shifters according to the desired direction of the two beams. The phase-shifted signals are then combined as input to the individual power amplifiers, which then feed into the individual microstrip antenna elements. Each of the 16 power amplifier devices used was a nonlinear MWT-173 Gallium Arsenide (GaAs) metal-semiconductor field-effect transistor (MESFET) nonlinear transistor model from Modelithics, biased at V_{DS} = 4.5 V and V_{GS} = -1.5 V. The input 1-dB compression point (P1dB) is $P_{\text{in,1dB}}$ = 14 dBm for this type of amplifier, and results in an output power of 20.07 dBm. Driving the device beyond P1dB results in gain reduction and nonlinear behavior with third-order intermodulation distortion, simply modeled by the previously described equation (3). The amplifier gain values vary based on factors which do include compression related to the input power, but which also include the load impedance and source impedance of the amplifier. The different mutual couplings of the different elements, which change based on the beam-steering angles, can cause the load impedances to vary between the different elements, resulting in gain values that vary greatly. The effect of varying impedance due to mutual coupling changes is thoroughly discussed and explained through visual plots in our recent conference paper on single-beam impedance tuning [14].

As discussed in the previous section, the excitations producing the two beams are fed into the individual antenna elements as given by (1), and the nonlinear power amplifiers cause unwanted IMD3 artifacts at the operating frequency ω_0 that translate into the unwanted beat beams. It should be noted that the various parameters used for the nonlinear devices in this simulation platform are not identical or directly related to those used in the simplified mathematical modeling of the nonlinear performance described in Section II (the Section II pictures are simply "cartoons" created to illustrate the basic concepts). To remove the beat beams at the fundamental frequency, the PA outputs must be modified such that the antenna fundamental-frequency input currents share the same relationships as the currents submitted to the amplifier inputs, which have been calculated to create the desired dual-beam array pattern. The proposed approach focuses only on the fundamental component of the output and input signal. While a more comprehensive approach, extending to minimize nonlinearity artifacts at all frequencies, would need to account for the entire time-domain signal, given the fact that multiple harmonic and intermodulation products are present in the amplifier output signal, examining and optimizing only the fundamental-frequency term shows effectiveness at reducing the fundamental-frequency beat beams. If it is desired to ensure the reduction nonlinearity artifacts at other frequencies, then a more in-depth method must be pursued. However, the method presented here

typically operates by performing impedance tuning to linearize amplifier performance; hence resulting in less significant nonlinearity products at other frequencies.

The approach to minimize beat beams at the fundamental frequency is accomplished by maintaining the same ratio of the amplifier output signal's fundamental frequency component to the input signal's fundamental frequency components across all of the array elements. The complex ratio κ_n is defined as the ratio of the input fundamental frequency-component current phasor to the output fundamental frequency-component current phasor for the amplifier in the nth array element:

$$\kappa_n = \frac{I_{i,n}}{I_{o,n}^{imd3}}. \tag{20}$$

Attempting to make the κ_n values the same for all array elements essentially attempts to ensure that the fundamental-frequency components of the output currents are identical complex constant multiples of their input currents. If the output phasors of all of the amplifier fundamental-frequency components are related to each other in the same way in amplitude and phase as the original signals (used as input currents), then the array factor and far-field pattern will be identical to the intended pattern at the fundamental-frequency. In such case, the fundamental-frequency array factor from the optimized-amplifier aperture, $AF_{corrected}(\theta)$ will contain only terms resulting from α_r and α_c terms at the elements, each modified by the complex multiplier $1/\kappa_n$:

$$AF_{corrected}(\theta) = \sum_{n=0}^{N-1} \frac{1}{|\kappa_n|} A_{r_n} e^{j(n[k_0 d sin(\theta) - (\alpha_r + \angle\kappa_n)])} + \sum_{n=0}^{N-1} \frac{1}{|\kappa_n|} A_{c_n} e^{j(n[k_0 d sin(\theta) - (\alpha_c + \angle\kappa_n)])}. \tag{21}$$

If the κ_n are all the same, then the array factor will be undistorted, and the spurious beams are eliminated at the fundamental frequency. Optimization of the PAs should therefore be performed to obtain all κ_n phasor values equal in magnitude and phase. In this case, the corrected feed excitation sent to the antenna will resemble the linear phasor excitation shown in (1), which does not cause spurious transmissions in the array pattern, and only the two intended RadCom beams will be transmitted.

To construct a procedure that allows optimization of the κ_n values to minimize fundamental-frequency beam distortion in real time, reconfigurable impedance tuners are placed between each PA and antenna element, as shown in Fig. 6. This reconfigurable matching network changes the phasor current $I_{o,n}^{imd3}$ that is fed to the nth antenna element. The current leaving the matching network is herein labeled as $I_{o,n}^{imd3'}$, and the modified value of κ_n used for the optimization is given by equation (9) with $I_{o,n}^{imd3'}$ replacing $I_{o,n}^{imd3}$. The reconfigurable matching network in each element between the PA device and antenna can intelligently tune each individual feed phasor signal $I_{o,n}^{imd3'}$ in to obtain identical modified values of κ_n across the elements, removing IMD3 effects from the fundamental-frequency array pattern. Fig. 7 shows this concept for the entire array. In the dual-beam scenario, equation (1) shows that each PA will be driven with a different input power level based on the different relative phases of the radar and communication terms, causing the linearity of the PAs in the different elements to vary. At these different drive levels, the gain and IMD3 levels will also vary significantly.

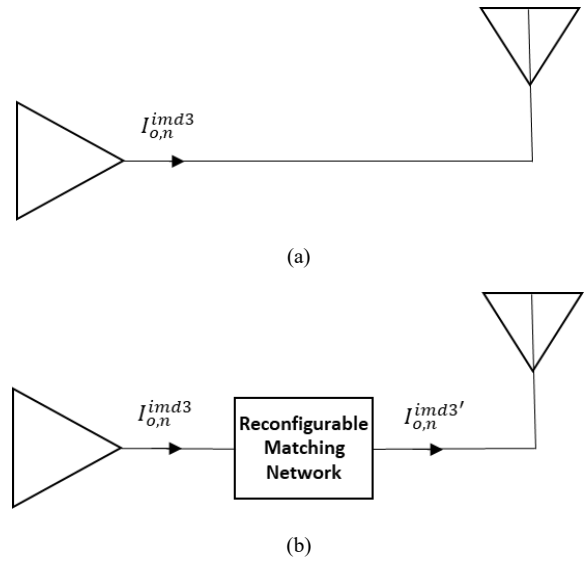

Fig. 6. (a) Antenna feed without matching network, (b) antenna feed with reconfigurable matching network.

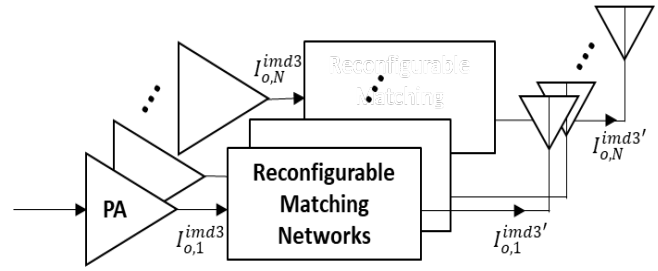

Fig. 7. Block diagram of element-wise array matching circuit configuration

Because an array providing two distinct beams often must transmit a significant amount of power from each array element, the power amplifier in each array element will consume significant supply power. Maximizing the power efficiency of each amplifier is thus crucial to overall efficient use of supply power. To accomplish this, the tuning algorithm also focuses on maximizing the gain of each element's power amplifier by tuning the load impedance. As such, the two goals of the optimization are the following: (1) ensure distortion in magnitude and phase of the current is as close to the same as possible between all array elements, and (2) ensure the current gain, described by the fundamental input and output terms, is as large as possible in each element. As aforementioned, this

method examines only the fundamental-frequency nonlinearity artifacts, so it is not a comprehensive nonlinearity-elimination method. However, it will be shown as follows to capably reduce unwanted beat beams at the fundamental frequency. Because the method typically results in the selection of element load impedances with greater linearity, it is expected that this method may also significantly reduce unwanted nonlinearity artifacts at other frequencies as well. It should also be noted that impedance tuners, which may be narrowband, may also provide undesirable results at harmonic frequencies unless a harmonic tuning approach is used, which is not considered in this paper pertaining to its effect on spatial-spectral nonlinearity artifacts.

IV. IMPEDANCE TUNING SIMULATION RESULTS

To demonstrate an impedance tuning approach using the ADS/Momentum co-simulation platform, a circuit model of an evanescent-mode cavity impedance tuner designed by Semnani [13] is placed between each of the 16 PA nonlinear transistor models and each of the 16 antenna elements in the ADS simulator. Fig. 8 shows the measured reflection coefficient values for different tuner settings on the Smith Chart at 3.55 GHz. The Smith Chart coverage is very extensive.

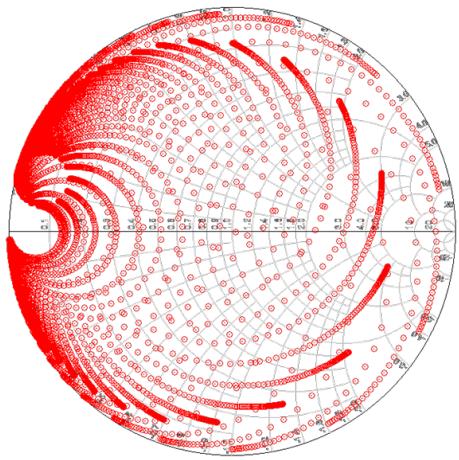

Fig. 8. Simulated impedance tuner [13] Smith Chart coverage at 3.55 GHz.

The simulation was constructed to provide 18.88 dBm available input power to the first "radar" component and 16.19 dBm available input power to the second "communication" component at each PA. The sources for the two beams are combined in parallel, causing their currents to add. The overall available power level of each PA varies with the relative phases of the radar and communication inputs. No input matching network design was performed for this simple experiment, so the input power values measured in the circuit schematic, representing the power delivered to the network, are lower than the available power values for those elements. A gradient descent optimization was applied directly in the ADS optimizer tool to tune the reconfigurable capacitors, modeling the resonator discs, in each tuner. As the optimization changes the impedance tuning settings, the complex values of κ_n are changed. The simulation optimizer is given two goals: minimizing the standard deviation of the κ_n phasor quantities, as defined by (20), and minimizing the individual magnitudes of the κ_n phasor quantities. Minimizing κ_n standard deviation ensures all phasor quantities are as identical as possible to restore the ideal array pattern. Minimizing $|\kappa_n|$ maximizes the amplifier gain and output power. The simulation was performed for three different dual-beam direction combinations. In each case, the results of impedance tuning are compared to untuned results, where the amplifier device output is connected directly to the antenna with no matching network present.

A. *DUAL-BEAM DIRECTIONS:* $\theta_r = -30°$ *AND* $\theta_c = +40°$

Following the optimizations in the ADS/Momentum simulator, the resulting elevation array pattern was compared with the unoptimized pattern. For the first combination of transmission directions ($\theta_r = -30°$ and $\theta_c = +40°$), the ideal array pattern with no PA device connected, possessing no IMD3 and therefore providing only linear phasor excitations (1), is shown in Fig. 9.

The ideal linear excitations cause the dual-beam array to transmit only two intended beams in the far-field, as expected. The magnitude of the beam at $\theta_r = -30°$ is 13.77 dBi and the magnitude of the beam at $\theta_c = +40°$ is 9.36 dBi. When a PA is connected to each antenna element, the IMD3 phasor signals of (3) cause two additional undesired beams to be transmitted in the far-field, as expected. The PA nonlinearities additionally distort the magnitude of the intended beams, since some of the power is now re-allocated to the two spurious beams. The IMD3 array pattern in Fig. 10(a) shows that the magnitude of the intended beam at $\theta_r = -30°$ is now 12.87 dBi, and the magnitude of the intended beam at $\theta_c = +40°$ is now 9.77 dBi. Additionally, the two spurious beat beams are visible: the magnitude of the beat beam at $\theta_{bb1} = -12°$ is 3.44 dBi, and the magnitude of the beat beam at $\theta_{bb2} = +21°$ is 2.37 dBi. Fig. 10(b) shows the far-field array pattern that is transmitted following the impedance tuning optimization, minimizing the size and vector standard deviation of κ_n. The optimized array pattern of Fig. 10(b), with impedance tuning applied, more closely resembles the ideal array pattern of Fig. 9. After impedance tuning, the magnitude of the beam at $\theta_r = -30°$ is 13.76 dBi, the magnitude of the beam at $\theta_c = +40°$ is 8.91 dBi, the magnitude of the first beat beam at $\theta_{bb1} = -12°$ is -5.70 dBi, and the magnitude of the second beat beam at $\theta_{bb2} = +21°$ is -15.23 dBi, indicating spurious beam suppression and a close restoration of the intended array pattern shape.

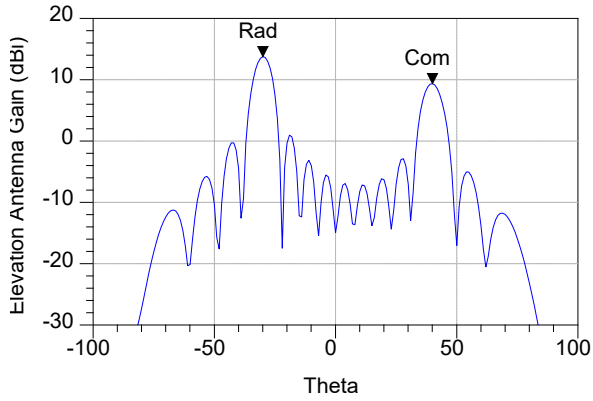

Fig. 9. Ideal elevation array parttern (dBi) without PAs: $\theta_r = -30°$, $\theta_c = +40°$.

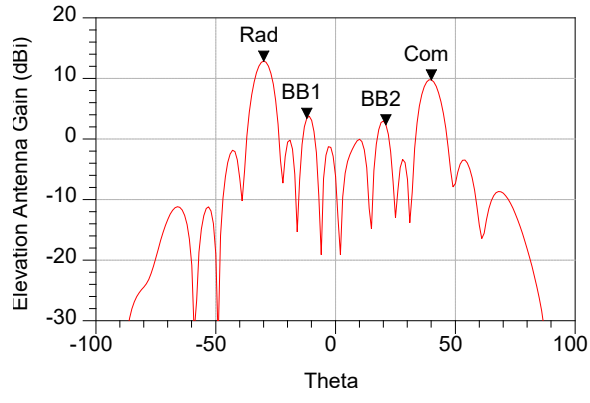

(a)

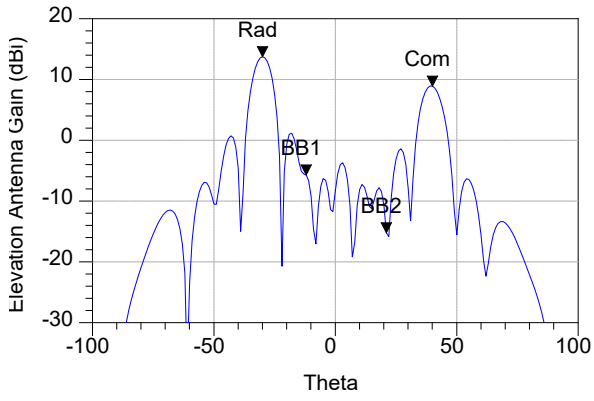

(b)

Fig. 10. (a) Elevation array pattern with un-tuned PA outputs: $\theta_r = -30°$, $\theta_c = +40°$, calculated $\theta_{bb1} = -12°$, calculated $\theta_{bb2} = +21°$, (b) elevation array pattern with tuned PA outputs: $\theta_r = -30°$ and $\theta_c = +40°$. $\theta_{bb1} = -12°$ and $\theta_{bb2} = +21°$ suppressed.

Table I provides a comparison of the main and beat beam antenna gain magnitudes for the ideal (no PA), untuned, and optimized cases, respectively. Table II shows an analysis of the κ_n IMD3 reversal factor element-wise magnitudes and phases, along with the associated current gain of each element. Since these κ_n values are significantly different in both magnitude and phase, the array element phasor excitations are different from the ideal excitations, causing far-field array pattern distortion, as shown in Fig. 10(a). The untuned $|\kappa_n|$ standard deviation is 0.13 and the untuned $\angle\kappa_n$ standard deviation is 10.59°. Impedance tuning can be implemented to lower the standard deviations of $|\kappa_n|$ and $\angle\kappa_n$, indicating that the effects of the IMD3 phasor excitations have been reversed before they are fed to the antenna elements. From Table III, $|\kappa_n|$ and $\angle\kappa_n$ are now much closer in value than the un-tuned values of Table II. Following impedance tuning, the $|\kappa_n|$ standard deviation is reduced to 0.07 and the $\angle\kappa_n$ standard deviation is reduced to 6.43°. This results in an array pattern in Fig. 10(b) that more closely resembles the ideal array pattern of Fig. 9. It can also be noted that the significantly low gains of some elements in the array (for example, element 2) are raised following impedance tuning. Tables II and III, with Fig. 10, show that impedance tuning profoundly improves array pattern integrity while maximizing the current gain of the array elements.

TABLE I

BEAM MAGNITUDES (DBI) FOR $\theta_r = -30°$ AND $\theta_c = +40°$

Array Pattern Case	θ_r Gain (dbi)	θ_c Gain (dbi)	θ_{BB1} Gain (dbi)	θ_{BB2} Gain (dbi)
IDEAL	13.77	9.36	-	-
IMD3	12.87	9.77	3.44	2.37
TUNED	**13.76**	**8.91**	**-5.70**	**-15.23**

TABLE II

UNTUNED κ_n VALUES FOR $\theta_r = -30°$ AND $\theta_c = +40°$

Element	$\lvert\kappa_n\rvert$	$\angle\kappa_n(°)$	Current Gain (dB)
1	0.29	-110.50	10.75
2	0.69	-102.07	3.22
3	0.49	-95.38	6.20
4	0.52	-93.29	5.68
5	0.44	-94.25	7.13
6	0.29	-145.83	10.75
7	0.55	-88.88	5.19
8	0.29	-113.10	10.75
9	0.91	-80.46	0.82
10	0.25	-139.93	12.04
11	0.54	-92.97	5.35
12	0.49	-103.61	6.20
13	0.22	-154.00	13.15
14	0.53	-90.25	5.51
15	0.29	-112.06	10.75
16	0.63	-94.72	4.01

As shown in Table III, impedance tuning provides every element with gain, and very similar magnitudes and phases of κ_n are observed between the array elements. Table I shows that the magnitudes of the main beams more closely resemble their ideal values.

TABLE III
TUNED κ_n VALUES FOR $\theta_r = -30°$ AND $\theta_c = +40°$

Element	$\lvert\kappa_n\rvert$	$\angle\kappa_n(°)$	Current Gain (dB)
1	0.47	-81.54	6.55
2	0.59	-65.68	4.58
3	0.44	-79.77	7.13
4	0.45	-75.82	6.94
5	0.45	-73.84	6.94
6	0.45	-81.17	6.94
7	0.58	-66.51	4.73
8	0.44	-76.52	7.13
9	0.61	-64.21	4.29
10	0.44	-79.31	7.13
11	0.45	-75.11	6.94
12	0.45	-74.53	6.94
13	0.46	-81.95	6.74
14	0.58	-63.68	4.73
15	0.44	-78.27	7.13
16	0.57	-80.62	4.88

B. DUAL-BEAM DIRECTIONS: $\theta_r = +10°$ AND $\theta_c = -15°$

The simulation experiment was repeated for a different combination of transmission directions: $\theta_r = +10°$ and $\theta_c = -15°$. For this scenario, the ideal array pattern is shown in Fig. 11. The magnitude of the beam at $\theta_r = +10°$ is 14.26 dBi, and the magnitude of the beam at $\theta_c = -15°$ is 10.83 dBi. Fig. 12(a) shows the array pattern with untuned nonlinear PA devices added, resulting in beam magnitudes of 13.36 dBi ($\theta_r = +10°$) and 11.22 dBi ($\theta_c = -15$). The magnitude of the first spurious beam at $\theta_{bb1} = -44°$ is -5.79 dBi, and the magnitude of the second spurious beam at $\theta_{bb2} = +37°$ is 0.73 dBi. As in the first scenario, connecting a compressed PA to each antenna element has disturbed the array pattern significantly.

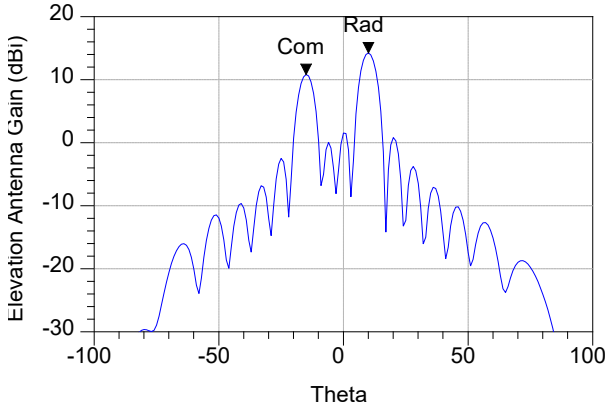

Fig. 11. Ideal elevation array pattern (dBi) without PAs: $\theta_r = +10°$, $\theta_c = -15°$.

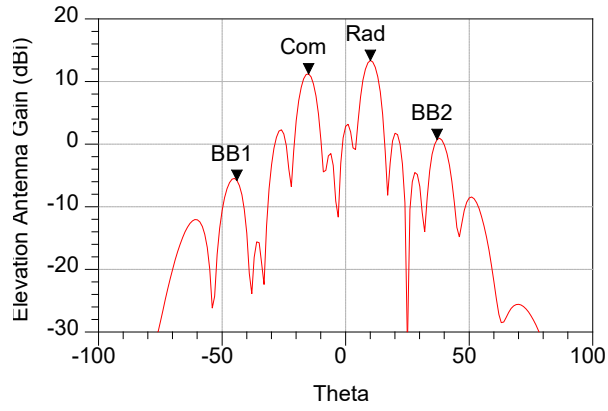

(a)

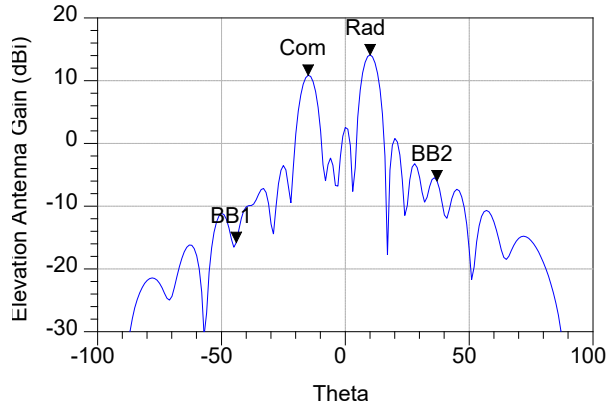

(b)

Fig. 12. (a) Elevation array pattern with un-tuned PA outputs: $\theta_r = +10°$, $\theta_c = -15°$, calculated $\theta_{bb1} = -44°$, calculated $\theta_{bb2} = +37°$; (b) elevation array pattern with tuned PA outputs: $\theta_r = +10°$ and $\theta_c = -15°$. $\theta_{bb1} = -44°$ and $\theta_{bb2} = +37°$ suppressed.

Impedance tuning was once again implemented using the gradient descent algorithm to lower the standard deviations of $\lvert\kappa_n\rvert$ and $\angle\kappa_n$, compensating for the effects of the IMD3 phasor excitations and providing the needed phasor element excitations based on the desired beam pattern. Fig. 12(a) shows the untuned array pattern with PAs included, and Fig. 12(b) shows the tuned far-field array pattern that is transmitted. The magnitude of the first main beam at $\theta_r = +10°$ in the tuned array is restored to 14.13 dBi, and the magnitude of the second main beam at $\theta_c = -15°$ is 10.87 dBi. The magnitude of the beat beam at $\theta_{bb1} = -44°$ is reduced to -15.79 dBi, and the magnitude of the beat beam at $\theta_{bb2} = +37°$ is reduced to -5.96 dBi, indicating successful spurious beam suppression. Tuning causes the array pattern (Fig. 12(b)) to more closely resemble the ideal array pattern of Fig. 11.

Table IV shows the beam magnitudes of each beam in the canonical, untuned, and tuned cases. The tuned-case dBi values of the two main beams are much closer to the ideal values than for the case where IMD3 is uncorrected. Table V shows the untuned κ_n IMD3 reversal factor element-wise magnitudes and phases for this set of main and spurious beam transmission directions. Table VI shows the κ_n magnitudes and phases following the impedance tuning optimization. Comparing Table VI to Table V shows that the κ_n values are much more similar in

the tuned case (Table VI), and that the PA current gain values are much more consistent in the tuned case.

TABLE IV
BEAM MAGNITUDES (DBI) FOR $\theta_r = +10°$ AND $\theta_c = -15°$

Array Pattern Case	θ_r Gain (dbi)	θ_c Gain (dbi)	θ_{BB1} Gain (dbi)	θ_{BB2} Gain (dbi)
IDEAL	14.26	10.83	-	-
IMD3	13.36	11.22	-5.79	0.73
TUNED	**14.12**	**10.87**	**-15.79**	**-5.96**

TABLE V
UNTUNED κ_n VALUES FOR $\theta_r = +10°$ AND $\theta_c = -15°$

Element	$\lvert\kappa_n\rvert$	$\angle\kappa_n(°)$	Current Gain (dB)
1	0.31	-116.53	10.17
2	0.27	-125.85	11.37
3	0.78	-98.84	2.16
4	0.71	-92.74	2.97
5	0.27	-128.62	11.37
6	0.31	-133.25	10.17
7	0.59	-93.13	4.58
8	0.76	-91.92	2.38
9	0.47	-95.35	6.56
10	0.27	-123.73	11.37
11	0.24	-125.58	12.40
12	0.79	-103.91	2.05
13	0.61	-93.54	4.29
14	0.22	-142.61	13.15
15	0.24	-144.64	12.40
16	0.69	-95.70	3.22

TABLE VI
TUNED κ_n VALUES FOR $\theta_r = +10°$ AND $\theta_c = -15°$

Element	$\lvert\kappa_n\rvert$	$\angle\kappa_n(°)$	Current Gain (dB)
1	0.46	-80.95	6.74
2	0.44	-77.38	7.13
3	0.56	-64.84	5.03
4	0.49	-64.77	6.20
5	0.44	-78.00	7.13
6	0.48	-79.26	6.38
7	0.41	-69.25	7.74
8	0.59	-66.62	4.58
9	0.46	-74.83	6.74
10	0.45	-81.31	6.94
11	0.44	-77.50	7.13
12	0.50	-64.90	6.02
13	0.54	-63.53	5.35
14	0.45	-77.46	6.94
15	0.47	-80.30	6.56
16	0.43	-77.32	7.33

C. *DUAL-BEAM DIRECTIONS:* $\theta_r = +50°$ *AND* $\theta_c = -50°$

For $\theta_r = +50°$ and $\theta_c = -50°$, the ideal array pattern is shown in Fig. 13. The magnitude of the first main beam at $\theta_r = +50°$ is 12.52 dBi and the magnitude of the second main beam at $\theta_c = -50°$ is 8.55 dBi. The array pattern for the system, including the untuned transistor devices with IMD3 effects, is shown in Fig. 14(a). With the amplifier distortion present, the magnitude of the first main beam at $\theta_r = +50°$ is 10.98 dBi, the magnitude of the second main beam at $\theta_c = -50°$ is 8.77 dBi, the magnitude of the first beat beam at $\theta_{bb1} = -17°$ is 1.80 dBi, and the magnitude of the second beat beam at $\theta_{bb2} = +17°$ is 3.48 dBi. This again results in a distorted array pattern shape (Fig. 14(a)) that is improved significantly by impedance tuning (Fig. 14(b)).

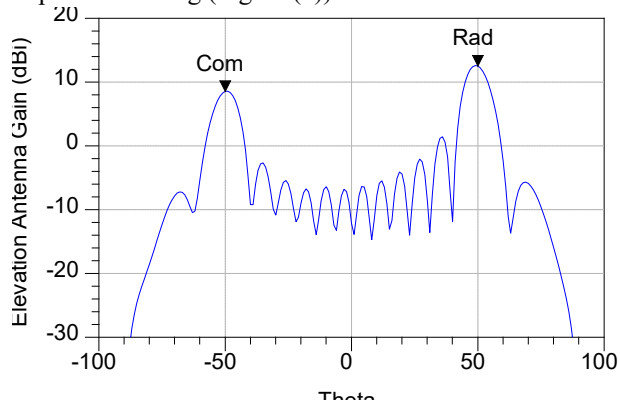

Fig. 13. Ideal elevation array pattern (dBi) without PAs: $\theta_r = +50°$, $\theta_c = -50°$.

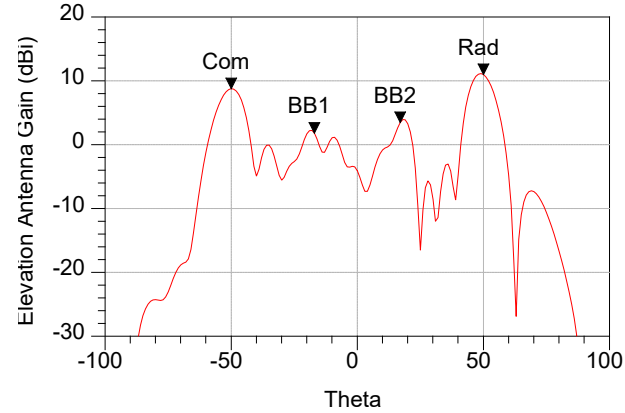

(a)

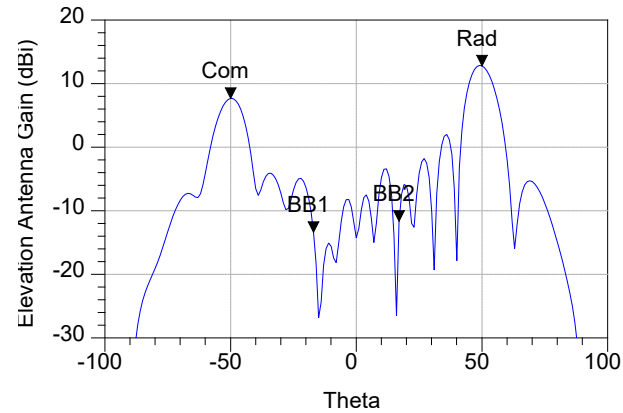

(b)

Fig. 14. (a) Elevation array pattern with un-tuned PA Outputs: $\theta_r = +50°$, $\theta_c = -50°$, calculated $\theta_{bb1} = -17°$, calculated $\theta_{bb2} = +17°$; (b) elevation array pattern with tuned PA outputs: $\theta_r = +50°$ and $\theta_c = -50°$. $\theta_{bb1} = -17°$ and $\theta_{bb2} = +17°$ suppressed.

Table VII shows the antenna gain magnitudes of the different beams for the ideal 16-element array pattern, the array pattern including the transistors without impedance tuning, and the array pattern with impedance tuning included. Impedance tuning allows very reasonable restoration of the radar and communication beams. Table VIII shows the κ_n element-wise magnitudes and phases for the untuned case, and Table IX shows the same information for the tuned case. The results again show that impedance tuning provides consistent κ_n magnitudes and phases between the elements, and that the PA current gain values are much more similar.

The three simulation experiments have demonstrated that impedance tuning can provide notable improvement in the array patterns when IMD3 distorts the array patterns from the ideal array pattern cases, even when the distortion is significant.

TABLE VII
BEAM MAGNITUDES (DBI) FOR $\theta_r = +50°$ AND $\theta_c = -50°$

Array Pattern Case	θ_r Gain (dbi)	θ_c Gain (dbi)	θ_{BB1} Gain (dbi)	θ_{BB2} Gain (dbi)
IDEAL	12.52	8.55	-	-
IMD3	10.98	8.77	1.80	3.48
TUNED	**12.81**	**7.69**	**-13.40**	**-11.64**

TABLE VIII
UNTUNED κ_n VALUES FOR $\theta_r = +50°$ AND $\theta_c = -50°$

Element	$\lvert\kappa_n\rvert$	$\angle\kappa_n(°)$	Current Gain (dB)
1	0.31	-110.81	10.17
2	0.41	-94.67	7.74
3	0.64	-86.53	3.88
4	0.54	-103.84	5.35
5	0.19	-101.44	14.42
6	0.39	-90.71	8.18
7	0.51	-85.31	5.85
8	0.51	-105.78	5.85
9	0.25	-124.88	12.04
10	0.28	-106.08	11.06
11	0.44	-96.77	7.13
12	0.53	-99.96	5.51
13	0.48	-100.23	6.38
14	0.32	-110.04	9.90
15	0.40	-93.98	7.96
16	0.58	-85.80	4.73

TABLE IX
TUNED κ_n VALUES FOR $\theta_r = +50°$ AND $\theta_c = -50°$

Element	$\lvert\kappa_n\rvert$	$\angle\kappa_n(°)$	Current Gain (dB)
1	0.49	-83.95	6.20
2	0.44	-79.2	7.13
3	0.60	-76.27	4.44
4	0.49	-76.89	6.20
5	0.48	-81.34	6.38
6	0.45	-80.53	6.94
7	0.57	-71.47	4.88
8	0.56	-71.14	5.04
9	0.46	-79.3	6.74
10	0.47	-80.89	6.56
11	0.52	-70.75	5.68
12	0.58	-69.7	4.73
13	0.44	-80.05	7.13
14	0.46	-81.71	6.74
15	0.41	-71.09	7.54
16	0.60	-54.34	4.44

V. COMPARISON OF IMPEDANCE TUNING WITH PREDISTORTION

Instead of using impedance tuning, Braithwaite [22] applies digital predistortion (DPD) to reduce the IMD3 beams that occur from PA nonlinearities in a dual-beam, shared-frequency system. DPD modules are applied for beam correction in the four transmitted beam directions: two for the intended linear beam directions, and two for the unintended beat beam directions. Each DPD module uses a third-order basis vector that is calculated for each beam to reverse the nonlinear effects. These basis vector waveforms for each beam are shown below, as provided in [22]:

$$\begin{aligned} b_{r_n} &= \left[\left|I_{r_n}\right|^2 + 2\cdot\left|I_{c_n}\right|^2\right]\cdot I_{r_n} \\ b_{c_n} &= \left[\left|I_{c_n}\right|^2 + 2\cdot\left|I_{r_n}\right|^2\right]\cdot I_{c_n} \\ b_{bb1_n} &= I_{r_n}^2\cdot I_{c_n}^* \\ b_{bb2_n} &= I_{c_n}^2\cdot I_{r_n}^*, \end{aligned} \tag{22}$$

where I_{r_n} and I_{c_n} are the current phasors for the radar and communications signals, respectively, from equation (1). The basis waveforms b_{r_n}, b_{c_n}, b_{bb1_n}, and b_{bb2_n} are the correction waveforms described in [22]. These must be designed based on the current phasors for the intended radar and communications signals to suppress the radiation transmissions at θ_{bb1} and θ_{bb2}. The DPD module signals for the four beam directions θ_r ,θ_c, θ_{bb1}, and θ_{bb2} are the following [22]:

$$\begin{aligned} I_{DPD,r_n} &= I_{r_n} + b_{r_n}\cdot\rho_{r_n} \\ I_{DPD,c_n} &= I_{c_n} + b_{c_n}\cdot\rho_{c_n} \\ I_{DPD,bb1_n} &= b_{bb1_n}\cdot\rho_{bb1_n} \\ I_{DPD,bb2_n} &= b_{bb2_n}\cdot\rho_{bb2_n}, \end{aligned} \tag{23}$$

where ρ_{r_n}, ρ_{c_n}, ρ_{bb1_n}, and ρ_{bb2_n} are the DPD coefficient vectors for each beam. The DPD coefficient vectors are used to weight the basis waveforms to create the desired correction PA input signal [22]. The predistorted phasor to be fed to each PA is summed together from (22) as follows,

$$I_{predist_n} = I_{DPD,r_n} + I_{DPD,c_n} + I_{DPD,bb1_n} + I_{DPD,bb2_n}. \quad (24)$$

This calculation results in a linear signal fed to the antenna elements after amplification.

To compare our impedance tuning method with predistortion, a Matlab/ADS co-simulation using this DPD technique was performed to verify that the predistortion calculations in (22)-(24) resulted in a corrected array pattern with beat beam suppression. The predistortion calculations were performed in Matlab, based on the current phasors for the intended transmission directions. The ρ_{r_n}, ρ_{c_n}, ρ_{bb1_n}, and ρ_{bb2_n} coefficients were calculated by the Matlab DPD system object using the PA input currents (1) and the PA output currents (15) recorded from ADS. The resulting predistorted signals (22) were then fed to each PA in ADS to the same transistor PAs as before. A fixed single-stub matching network was used on each element to match the driven element PA load impedances for the simplest beam condition at the broadside scan angle: ($\theta_r = \theta_c = 0°$). The fixed single-stub matching was designed with the same input power values to the radar and communication components as the experiments in the previous section. Unlike the impedance tuning scenario, this network is not tuned as the beam angle is changed, but is held constant during the entire experiment. Fig. 15 shows the resulting corrected array pattern when predistortion is applied prior to amplification, with fixed matching networks on the PAs, for $\theta_r = -30°$ and $\theta_c = +40°$. These are the same transmission angles as in Figs. 9-10. An analysis of the κ_n metric for the case of predistortion is presented in Table X. The κ_n magnitudes and phases show significant differences compared to the results of impedance tuning shown in Table III. In predistortion, the input waveforms are adjusted to compensate for amplifier nonlinearities and the nonlinearities are left unchanged, whereas impedance tuning focuses on linearizing the amplifier and does not change the inputs. In Fig. 15, as a result of predistortion, the magnitude of the first spurious beam at $\theta_{bb1} = -12°$ is suppressed to -4.64 dBi and the magnitude of the second spurious beam at $\theta_{bb2} = +21°$ is suppressed to -5.48 dBi. For comparison, the impedance tuning experiments of the preceding section provided suppression of the first spurious beam $\theta_{bb1} = -12°$ to -5.70 dBi and suppression of the second spurious beam at $\theta_{bb2} = +21°$ to -15.23 dBi. In this experiment, predistortion indeed provided significant suppression of the beat beams, but did not suppress either of the beat beams as well as impedance tuning for this beam angle combination.

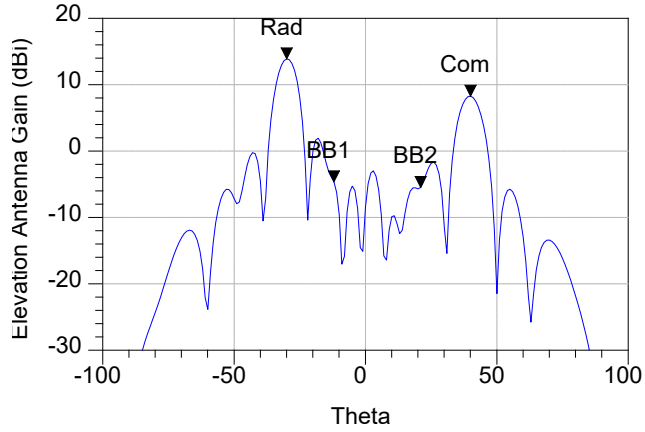

Fig. 15. Predistortion array pattern correction for: $\theta_r = -30°$ and $\theta_c = +40°$. $\theta_{bb1} = -12°$ and $\theta_{bb2} = +21°$ suppressed.

The individual PA current gain values are shown in Table X. Unlike the impedance tuning method, predistortion is not designed to maximize or homogenize the current gain values of the individual element PAs, but is focused solely on linearization. Since, in the simple case of predistortion considered in this comparison, the predistortion approach modifies the element inputs to accomplish the desired beam pattern and does not adjust the amplifiers, the resulting element current gain values of the PAs after predistortion is applied vary widely (Table X) as compared to impedance tuning (Table III). This is expected to cause a wide variation in power-added efficiency of the PAs as well. In both cases, back-off of many PA input power values is necessary to establish the beam pattern, but impedance tuning can make the best of the situation by adjusting to maximize element current gain, whereas the impedance matching of the predistortion method is fixed, and therefore cannot be adjusted to compensate. Since only the input waveform can be adjusted in the predistortion method, little flexibility exists to address gain and efficiency issues in real time.

Predistortion and impedance tuning were also compared for the other scan angle directions addressed in Figs. 11-14. For $\theta_r = -30°$ and $\theta_C = +40°$, the linear average element current gain was 8.51 dB in the untuned case, and 6.54 dB for impedance tuning. With predistortion, the linear average element PA current gain was 8.19 dB. This average current gain is similar to the untuned case from the previous section.

While the impedance tuning method addresses both linearity and efficiency issues in real time, it can be combined with predistortion to provide an overall benefit in some cases. To test the combination of impedance tuning and predistortion, impedance tuning was performed first, followed by predistortion, with the same Matlab input signal calculations applied as in the standalone case. Fig. 16 shows the array pattern results from combining predistortion and impedance tuning for $\theta_r = -30°$ and $\theta_c = +40°$. The κ_n magnitudes and phases, as well as current gain values, are recorded in Table XI. As shown in

Table XI, the combination of predistortion and impedance tuning resulted in a linear average element current gain of 9.42 dB, compared to linear average element current gain of 6.54 dB for standalone impedance tuning. The standard deviation of the current gain is largest for the untuned case (1.20 A/A) and smallest for the impedance tuning case (0.1980 A/A), as might be expected. Also, as expected, the standard deviations for predistortion (0.73 A/A) and predistortion-plus-impedance-tuning (0.49 A/A) fall in between these extremes. Since, in the predistortion-plus-impedance-tuning case, predistortion was performed after impedance tuning, the final element current gains vary more widely than for applying only impedance tuning. While it does lower the variations of current gain by increasing the total input current on several of the elements, the current gains vary more widely than when starting from the untuned case. Fig. 16 shows that the spurious beams were successfully suppressed, as in the case with standalone predistortion and standalone impedance tuning.

TABLE X
PREDISTORTION κ_n VALUES FOR $\theta_r = -30°$ AND $\theta_c = +40°$

Element	$\lvert\kappa_n\rvert$	$\angle\kappa_n(°)$	Current Gain (dB)
1	0.62	-36.25	4.15
2	0.31	-14.55	10.17
3	0.51	-13.27	5.85
4	0.36	-9.36	8.87
5	0.37	-3.89	8.64
6	0.49	-12.85	6.20
7	0.30	-4.56	10.46
8	0.60	-36.26	4.44
9	0.31	-15.31	10.17
10	0.51	-13.16	5.85
11	0.36	-8.90	8.87
12	0.37	-4.44	8.64
13	0.49	-13.49	6.20
14	0.31	-3.41	10.17
15	0.61	-35.25	4.29
16	0.24	-13.37	12.40

The same experiment was performed for the other scan angle combinations using the combined impedance tuning and predistortion method. Tables XII, XIII, and XIV provide a summary of the performance of the impedance tuning, predistortion, and combined methods. Table XII shows that applying impedance tuning for θ_r = -30° and θ_c = +40° provides an increase of radiated powers to 29.33 dBm for the radar beam and 24.49 dBm for the communications beam. Assuming radar and communications applications for the first and second beams, respectively, these power values result in a 5.62% improvement in radar range and a 22.20% improvement in communication range when compared to predistortion. Furthermore, impedance tuning provides better beat-beam suppression than predistortion. If the combined method is used, the radiated power increases to 29.87 dBm (8.95% radar range increase compared to predistortion) for the radar beam and the 25.06 dBm for the communications beam (30.47% communication range increase compared to predistortion).

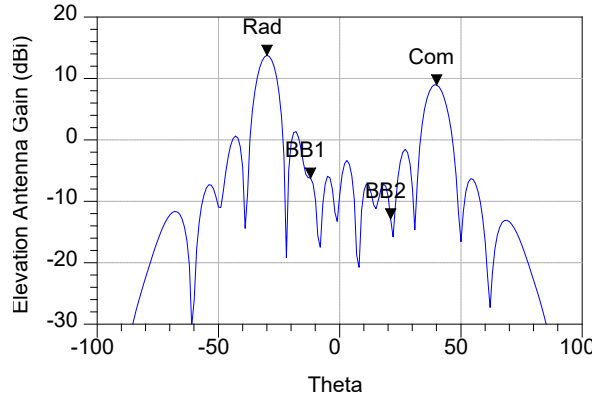

Fig. 16. Predistortion and impedance tuning array pattern correction for: $\theta_r = -30°$ and $\theta_c = +40°$. $\theta_{bb1} = -12°$ and $\theta_{bb2} = +21°$ suppressed.

TABLE XI
PREDISTORTION AND IMPEDANCE TUNING κ_n VALUES FOR $\theta_r = -30°$ AND $\theta_c = +40°$

Element	$\lvert\kappa_n\rvert$	$\angle\kappa_n(°)$	Current Gain (dB)
1	0.44	63.11	7.13
2	0.32	73.68	9.90
3	0.38	72.16	8.40
4	0.30	77.34	10.46
5	0.31	80.48	10.17
6	0.37	73.34	8.64
7	0.31	86.98	10.17
8	0.44	48.59	7.13
9	0.32	61.02	9.90
10	0.38	74.01	8.40
11	0.30	78.09	10.46
12	0.31	80.14	10.17
13	0.38	73.23	8.40
14	0.32	90.03	9.90
15	0.43	54.60	7.33
16	0.24	69.25	12.40

The experiment was repeated for the other scan angle combinations. Again assuming radar and communication applications, for $\theta_r = +10°$ and $\theta_c = -15°$ (Table XIII), impedance tuning provided a range increase of 0.69% for the radar beam and 11.94% for the communications beam compared to standalone predistortion. The combined method provided a range increase of 3.10% for the radar beam and a 17.75% range increase for the communications beam compared to standalone predistortion. For $\theta_r = +50°$ and $\theta_c = -50°$ (Table XIV), impedance tuning provided a range increase of 14.03% for the radar beam and a 34.11% range increase for the communications beam compared to standalone predistortion. The combined method provided a range increase of 16.68% for the radar beam and a 42.06% range increase for the communications beam compared to standalone predistortion. Impedance tuning is therefore essential in increasing range capabilities and suppressing spurious beams in a dual-beam system.

Overall, these simulation experiments have demonstrated that impedance tuning can increase range capability while providing excellent beat-beam suppression. Combining impedance tuning and predistortion provides many of the benefits of impedance tuning, with additional linearization capabilities applied through the ability to adjust the element input waveforms.

TABLE XII
RADIATED POWER AND SPURIOUS BEAM LEVELS
$\theta_r = -30°$ AND $\theta_c = +40°$

Method	Radiated Power (dBm) θ_r	Radiated Power (dBm) θ_c	θ_{bb1} Gain (dBi)	θ_{bb2} Gain (dBi)
Predistortion	28.38	22.75	-4.64	-5.48
Impedance Tuning	29.33	24.49	-5.70	-15.23
Combination	29.87	25.06	-6.24	-12.87

TABLE XIII
RADIATED POWER AND SPURIOUS BEAM LEVELS
$\theta_r = +10°$ AND $\theta_c = -15°$

Method	Radiated Power (dBm) θ_r	Radiated Power (dBm) θ_c	θ_{bb1} Gain (dBi)	θ_{bb2} Gain (dBi)
Predistortion	29.88	25.76	-9.38	-5.93
Impedance Tuning	30.00	26.74	-15.79	-5.96
Combination	30.41	27.18	-14.07	-5.23

TABLE XIV
RADIATED POWER AND SPURIOUS BEAM LEVELS
$\theta_r = +50°$ AND $\theta_c = -50°$

Method	Radiated Power (dBm) θ_r	Radiated Power (dBm) θ_c	θ_{bb1} Gain (dBi)	θ_{bb2} Gain (dBi)
Predistortion	25.96	20.57	-3.08	-1.25
Impedance Tuning	28.24	23.12	-13.40	-11.64
Combination	28.64	23.62	-10.11	-14.42

VI. CONCLUSIONS

Load-impedance tuning of power amplifiers in phased-array elements has been demonstrated as a solution to eliminate undesired, spurious beat beams in the transmission pattern while maximizing element amplifier gain. A joint circuit and electromagnetic simulation platform was used to demonstrate an impedance tuning approach to maximize output power and minimize the spurious beat beams for a 16-element, $\lambda/2$ spaced, microstrip linear array. The use of the IMD3 reversal factor provided a significant improvement in the dual-beam array pattern from the untuned IMD3 array pattern caused by third-order PA nonlinearities for multiple beam angles in same-frequency, dual-beam radar-communications transmission examples. Comparison of the tuned array pattern to the untuned array pattern including the results of amplifier nonlinearities, as well as to the ideal array pattern, shows that the array pattern can be improved to restore the intended relative amplitudes of the two beams, suppress the unintended spurious beat beams, and increase transmission range in the desired beam directions. Impedance tuning was also shown to have an advantage over predistortion because it focuses on maximizing element current gain and linearity, providing increased range capabilities for both desired beams while also minimizing the beat beams. Combining the impedance tuning and predistortion techniques can cause further reduction of the spurious beat beams in some cases. As such, impedance tuning is recommended as a critical component of dual-beam array transmissions to maximize amplifier gain and efficiency while significantly reducing the beat beams. Impedance tuning, as presented in this work, provides a useful new tool for the reduction of undesirable distortions in multi-beam, spatially diverse transmissions.

ACKNOWLEDGMENTS

The authors wish to thank Keysight Technologies for donation of the Advanced Design System software as well as Modelithics for donation of nonlinear transistor model libraries to Baylor University through the Modelithics University Program. The authors are also grateful to Profs. Dimitrios Peroulis and Abbas Semnani for providing the impedance tuner model used in this paper for simulations.

REFERENCES

[1] P.M. McCormick, S.D. Blunt, and J.G. Metcalf, "Simultaneous Radar and Communications Emissions from a Common Aperture, Part I: Theory," 2017 IEEE Radar Conference, Seattle, Washington, May 2017.

[2] W.A. Sandrin, "Spatial Distribution of Intermodulation Products in Active Phased Array Antennas," *IEEE Transactions on Antennas and Propagation*, Vol. 21, No. 6, November 1973, pp. 864-868.

[3] E.G. Larsson and L. Van Der Pierre, "Out-of-Band Radiation From Antenna Arrays Clarified," *IEEE Wireless Communications Letters*, Vol. 7, No. 4, August 2018, pp. 610-613.

[4] C. Hemmi, "Pattern Characteristics of Harmonic and Intermodulation Products in Broad-Band Active Transmit Arrays," *IEEE Transactions on Antennas and Propagation*, Vol. 50, No. 6, June 2002, pp. 858-865.

[5] R.L. Haupt, "Antenna Arrays in the Time Domain: An Introduction to Timed Arrays," *IEEE Antennas and Propagation Magazine*, Vol. 59, No. 3, June 2017, pp. 33-41.

[6] C. Mollen, U. Gustavsson, T. Eriksson, and E.G. Larsson, "Spatial Characteristics of Distortion Radiated From Antenna Arrays With Transceiver Nonlinearities," *IEEE Transactions on Wireless Communications*, Vol. 17, No. 10, October 2018, pp. 6663-6679.

[7] A.I. Zaghloul, O. Kilic, and E.C. Kohls, "System Aspects and Transmission Impairments of Active Phased Arrays for Satellite Communications," *IEEE Transactions on Aerospace and Electronic Systems*, Vol. 43, No. 1, January 2007, pp. 176-186.

[8] S.L. Loyka, "The Influence of Electromagnetic Environment on Operation of Active Array Antennas: Analysis and Simulation Techniques," *IEEE Antennas and Propagation Magazine*, Vol. 41, No. 6, December 1999, pp. 23-39.

[9] M. Obermier and E.J. Powers, "The Effects of Nonlinear High Power Amplifiers on Space Based Phased Array Antenna Patterns," 2000 International Conference on Phased Array Systems and Technology, Dana Point, California, May 2000, pp. 45-48.

[10] T. Kaho, T. Nakagawa, K. Araki, and K. Horikawa, "Carrier Power to Intermodulation-Distortion Power-Ratio-Increasing Technique in Active Phased-Array Antenna Systems," *IEEE Transactions on Microwave Theory and Techniques*, Vol. 50, No. 12, December 2002, pp. 2987-2994.

[11] B. Rupakula and G. Rebeiz, "Third-Order Intermodulation Effects and System Sensitivity Degradation in Receive-Mode 5G Phased Arrays in the Presence of Multiple Interferers," *IEEE Transactions on Microwave Theory and Techniques*, Vol. 66, No. 12, December 2018, pp. 5780-5795.

[12] A. Semnani, M. Abu Khater, Y.-C. Wu, and D. Peroulis, "An Electronically Tunable High-Power Impedance Tuner with Integrated Closed-Loop Control," *IEEE Microwave and Wireless Components Letters*, Vol. 27, No. 8, July 2017, pp. 754-756.

[13] A. Semnani, G.S. Shaffer, M.D. Sinanis, and D. Peroulis, "High-Power Impedance Tuner Utlising Substrate-Integrated Evanescent-Mode Cavity Technology and External Linear Actuators," *IET Microwaves, Antennas & Propagation*, Vol. 13, No. 12, October 2019, pp. 2067-2072.

[14] P. Rodriguez-Garcia, J. Sifri, C. Calabrese, C. Baylis and R. J. Marks, "Range Improvement in Single-Beam Phased Array Radars by Amplifier Impedance Tuning," 2021 IEEE Texas Symposium on Wireless and Microwave Circuits and Systems, Waco, Texas, May 2021.

[15] A. O'Connor and D. Rabideau, "Dual-Beam Transmit from Shared Aperture with Constant Envelope Constraint," 2019 IEEE Radar Conference, Boston, Massachusetts, April 2019.

[16] K. Yamauchi, M. Nakayama, Y. Ikeda, Y. Isota and T. Takagi, "Novel Reduction Technique of the Non-Linear Distortion at the Receiving Point in the Multi-Beam Active Phased Array Antenna," *2005 Asia-Pacific Microwave Conference Proceedings*, Suzhou, 2005.

[17] E. Lier and A. Cherrette, "An Intermodulation Suppression Technique for Transmit Active Phased Array Satellite Antennas with Multiple Shaped Beams," *IEEE Transactions on Antennas and Propagation*, Vol. 53, No. 5, pp. 1853-1858, May 2005.

[18] K.G. Johannsen, "Scan Beam Antenna Intermodulation Improvement Due to Spatial Dispersion," *IEEE Transactions on Aerospace and Electronic Systems*, Vol. AES-23, No. 4, pp. 543-557, July 1987.

[19] R.L. Haupt and M.D. Weiss, "Power Amplifier Models for Multi-Beam Wideband Active Transmit Arrays," *2014 IEEE Antennas and Propagation Society International Symposium (APSURSI)*, Memphis, Tennessee, 2014, pp. 1750-1751.

[20] N. Peccarelli, B. James, R. Irazoqui, J. Metcalf, C. Fulton, and M. Yeary, "Survey: Characterization and Mitigation of Spatial/Spectral Interferers and Transceiver Nonlinearities for 5G MIMO Systems," *IEEE Transactions on Microwave Theory and Techniques*, Vol. 67, No. 7, July 2019, pp. 2829-2846.

[21] Z. Dunn, M. Yeary, C. Fulton, and R. Rincon, "Impedance-Dependent Wideband Digital Predistortion of Solid-State Radar Amplifiers," *IEEE Transactions on Aerospace and Electronic Systems*, Vol. 53, No. 5, October 2017, pp. 2290-2303.

[22] R.N. Braithwaite, "Amplifier Nonlinearities in an Antenna Array During Spatially Multiplexed Transmissions," 2020 IEEE Radio and Wireless Symposium, San Antonio, Texas, January 2020.

[23] C. Baylis, M. Fellows, L. Cohen, and R.J. Marks II, "Solving the Spectrum Crisis: Intelligent, Reconfigurable Microwave Transmitter Amplifiers for Cognitive Radar," *IEEE Microwave Magazine*, Vol. 15, No. 5, July 2014, pp. 94-107.

[24] A. Egbert, A. Goad, C. Baylis, A. Martone, B. Kirk, and R.J. Marks II, "Continuous Real-Time Circuit Reconfiguration to Maximize Average Output Power in Radar Transmitters," accepted for publication in *IEEE Transactions on Aerospace and Electronic Systems*, July 2021.

[25] F. Sechi and M. Bujatti, *Solid-State Microwave High-Power Amplifiers*, Artech House, 2009.

[26] B. James and C. Fulton, "Decorrelation and Mitigation of Spurious Products in Phased Arrays with Direct Conversion Transceivers," 2015 IEEE MTT-S International Microwave Symposium, Phoenix, Arizona, May 2015.